CCFE
CULHAM CENTRE FOR FUSION ENERGY

UK Atomic Energy Authority

UKAEA-CCFE-PR(19)35

A.J. Cackett, C.D. Hardie, J.J.H. Lim, E. Tarleton

Spherical indentation of copper: crystal plasticity vs. experiment

Spherical indentation of copper: crystal plasticity vs. experiment

A.J. Cackett, C.D. Hardie, J.J.H. Lim, E. Tarleton

This is a preprint of a paper submitted for publication in Materialia

Spherical indentation of copper: crystal plasticity vs. experiment

A.J. Cackett[a,b], C.D. Hardie[a,c], J.J.H. Lim[a], E. Tarleton[c,*]

[a] *UK Atomic Energy Authority, Culham Science Centre, Oxfordshire OX14 3DB, UK*
[b] *School of Engineering and Materials Science, Queen Mary University of London, Mile End Road, London E1 4NS*
[c] *Department of Materials, University of Oxford, Parks Road, OX1 3PH, UK*

Abstract

We analyse spherical nanoindentation of single crystal copper using two different indenter tips of radii 7.4 and 27 μm. The surface deformation surrounding the indents was measured using atomic force microscopy and the elastic rotation fields under the indents were measured using electron diffraction and transmission techniques. Using the measured load-displacement, surface relief, plastic zone size and elastic rotation field removed the ambiguity in the optimal slip and hardening law parameters in a three parameter strain gradient crystal plasticity model. In addition to geometrically necessary dislocations, other hardening mechanisms (source starvation, statistically stored dislocations) contribute to the size effect.

Keywords: spherical nanoindentation, crystal plasticity, TKD, EBSD, TEM

Nanoindentation is a popular technique to measure the mechanical properties of materials, especially for thin films [1] or where sample size is limited [2]. There are some clear benefits to this technique; unlike other small-scale testing methods, such as micro-cantilever bending [3] or micro-pillar compression [4], nanoindentation is less resource intensive, fully automated with modern instruments and highly consistent with established uncertainties. Indentation with the spherical tip geometry offers several additional advantages. Unlike indentation using sharp self-similar geometries (e.g. Berkovich), the strain imposed by spherical indentation varies as a function of depth. Thus, initial contact using spherical indenters is usually elastic, transitioning to elastic-plastic and fully plastic as the indent progresses. This provides the ability to measure the full stress-strain response and observe a range of material behaviour that is inaccessible with other tip geometries. From these curves it is possible to infer conventional properties such as yield stress and work hardening with correlation to uniaxial tensile test results [5, 6]. The spherical geometry lends itself to modelling since it avoids the high strains (and therefore numerical instabilities) associated with pyramidal tips and enables the reduction of the model by use of symmetry boundary conditions.

Interpretation of nanoindentation results and associated data analysis is not trivial. Tests are increasingly combined with modelling and simulation in order to both interpret the measured data and provide rigorous calibration and validation of material models. Data now accessible with experiments includes the load displacement response, surface sink-in/pile-up, sub-surface lattice rotations, and plastic zone size. This rich data set provides a means of validating theory and computational approaches such as discrete dislocation plasticity and crystal plasticity (CP). CP naturally incorporates plastic anisotropy and lattice rotation effects and so is well suited to simulate the experimental data available from indentation. Numerous previous combined experimental/modelling studies have been performed. Vickers and Berkovich nanoindentation of single crystal annealed and strain-hardened copper were simulated using J_2 and CP models [7]. Wedge indentation of copper was simulated using CP by Kysar et al. [8] who observed discontinuities in lattice rotation with a high geometrically necessary dislocation (GND) density. The surface pile-up in nano and micro indentation of Cu has been examined for directions not aligned with the crystal and the imprint topography around the indent was simulated [9]. A CP model for nanoindentation in copper has also been calibrated using molecular dynamics and discrete dislocation plasticity simulations [10]. The load and pressure under the nanoindent in copper were found to be highest for (111) and lowest for (100) orientations [11].

*Corresponding author
Email address: edmund.tarleton@materials.ox.ac.uk (E. Tarleton)

The deformation induced rotation pattern under conical indent planes has been investigated using EBSD and serial sectioning on (111) planes in combination with CP simulations [12, 13].

In this paper, we analyse single crystal copper with a surface normal along [010] indented with spherical tips of radii $R = 7.4\ \mu$m and $R = 27\ \mu$m, which are referred to here as the small and large tip respectively. Atomic force microscopy (AFM) was used to measure the surface relief surrounding the indent. Additionally, electron backscatter diffraction (EBSD) and transmission Kikuchi diffraction (TKD) were used to observe a cross-section of the plastic zone under the indent. TKD is a relatively new technique which offers higher spatial resolution than EBSD [14–16]. It was applied in this work to the smaller indent to resolve the deformation over the plastic zone of a few microns with sufficient resolution. This was compared with cross-sectional transmission electron microscopy (TEM) imaging, which provides a direct view of the dislocation structure induced during indentation. Simulations were performed with a physically based strain gradient CP model which had a minimal number of parameters, as listed in Table 1. The parameters were adjusted to match the load displacement response, residual free surface deformation from AFM, and residual lattice rotations from EBSD for the large indent only. The small indent was then simulated and the predictions of the model compared with the experimental data to check the validity of the model.

The raw load-displacement data for both the small ($R = 7.4\ \mu$m) and large ($R = 27\mu$m) indents, up to a strain of $\varepsilon = 0.2$, were automatically corrected for frame compliance and the load zero point, i.e. point of first contact between indenter and sample surface. To calibrate the model to the large indent the two free parameters in the slip rate law and the one free parameter in the hardening law; A, B and C in equations (1) and (2) were adjusted. For a slip system k the crystallographic slip rate was assumed to be [17]

$$\dot{\gamma}^k = A \sinh\left(B(|\tau^k| - \tau_c^k(\rho_c^k))\right) \mathrm{sgn}(\tau^k) \qquad (1)$$

with a critically resolved shear stress (CRSS),

$$\tau_c^k(\rho_c^k) = \tau_c^0 + C\mu b \sqrt{\rho_c^k}, \qquad (2)$$

τ_c^0 is the initial CRSS and ρ_c^k is the GND density cutting the slip plane. Further details are in the supplementary material. The optimal simulated curves are shown superimposed on the measured load displacement response in Figure 1. A small pop-in event can be seen in the small indent data, where a sudden increase in displacement at constant load is evident. This response is typical of indentation into material that has a low initial dislocation source density [18].

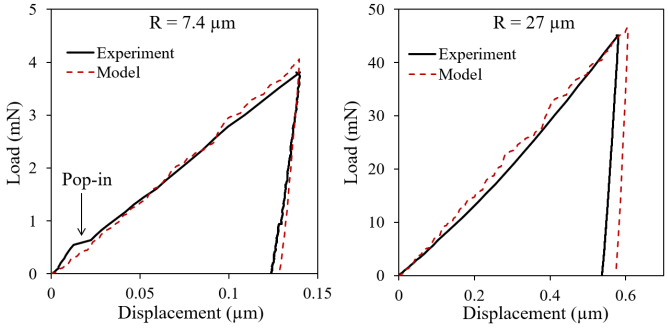

Figure 1: Experimental load displacement data (black solid lines) and optimised CP simulations (red dashed lines) for the small ($R = 7.4\ \mu$m) and large ($R = 27\ \mu$m) tips.

As can be seen in Figure 2 there is good agreement between the size of the measured and simulated surface profile maps. In both cases the position of the pile-up lobes and residual indent areas are remarkably similar. However, the model overestimates the maximum surface height of the pile-up (123 nm compared to a measured value of 89.4 nm for the large indent, and 29.1 nm compared to 16.5 nm for the small indent).

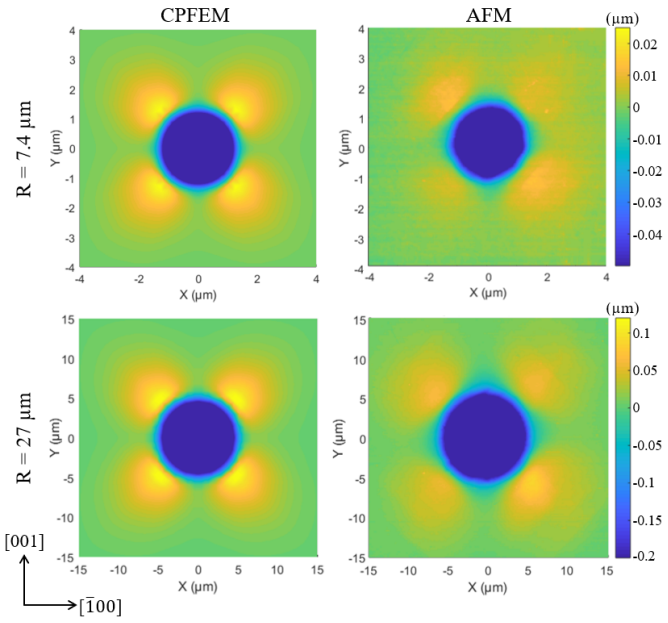

Figure 2: AFM (010) surface profile maps for the large (top row) and small (bottom row) indents with comparative result from the CP model.

The load-displacement response and residual deformation on the free surface around the indent obtained from AFM are often the only data used to calibrate the slip law

Material parameters	Small indent	Large indent	Description
A	2×10^{-6} s^{-1}	5×10^{-5} s^{-1}	slip law fitting constant
B	0.2 MPa^{-1}		slip law fitting constant
C	0.05		obstacle strength
τ_c^0	1 MPa		initial CRSS
b	2.55×10^{-4} μm		Burgers vector magnitude
E	66.7 GPa		Young's modulus
G	75.4 GPa		shear modulus
ν	0.42		Poisson's ratio
Geometry	**Small indent**	**Large indent**	**Description**
R	7.4 μm	27 μm	indenter tip radius
L	41 μm	150 μm	cube side length
w	0.25 − 3.0 μm	1.0 − 10 μm	element size range
U	0.14 μm	0.61 μm	indentation depth

Table 1: Parameters used to simulate indentation into single crystal Cu

[19]. Here we also use the subsurface deformation under the indent when calibrating the slip law parameters for the large indent. A side-by-side comparison between the measured and simulated rotation maps for both indent sizes are shown in Figure 3. TKD was performed for the smaller indent and EBSD for the larger indent, using step sizes of 13 nm and 50 nm respectively. In these maps the usual right hand convention is used so that positive values (red on the colour scale) indicate an anti-clockwise rotation when looking down the rotation axis ($[\bar{1}0\bar{1}]$, which is pointing out of the page in Figure 3) and negative values (blue on the colour scale) are clockwise. There is good agreement for the large indent, however under the small indent the region of high residual lattice rotation region measured using TKD is shallower than predicted by the model. This is unexpected as the load-displacement and surface deformation were in good agreement.

To accommodate deformation during indentation, dislocations must be generated in the crystal lattice. The density and distribution of these dislocations is dependent on the material and its orientation as well as the indenter tip size and its displacement into the surface. A bright-field TEM micrograph taken of the indent cross-section is shown in Figure 4(a), where a dense network of dislocations below the residual imprint can clearly be seen. Note that the image shown is in fact a negative of the original bright-field image in order to enhance the appearance of the dislocations. Slip traces can be seen due to the $[011](\bar{1}\bar{1}1)$ and $[\bar{1}10](\bar{1}\bar{1}1)$ slip systems that are both along $[\bar{1}21]$ at 54.7° to the horizontal axis, which is along $[\bar{1}01]$. Similarly the trace of the $[110](1\bar{1}\bar{1})$ and $[01\bar{1}](1\bar{1}\bar{1})$ slip systems are along $[12\bar{1}]$ at an angle of 125° to the horizontal. The plastic zone size extends much further into the material than would be inferred from TKD and CP. which are in good agreement with a localised GND density underneath the indent (Figures 4 (b) and (c)).

A summary of the experimental data is as follows. The load displacement data are in good agreement between experiment and model, as shown in Figure 1. The size of the contact area and pile-up area were also comparable between experiment and simulation for both tips, with surface relief surrounding the residual indent in the form of four pile-up lobes extending along the $\langle 101 \rangle$ directions. However the measured height of the pile-up was less than predicted by the simulation. Finally, the sign and spatial distribution of the residual elastic rotations were in good agreement for the large tip (Figure 3) and reasonable agreement for the small tip, although the model predicts a rotation field over a larger area than measured with TKD.

The model included three parameters which were used to fit the load displacement data with the experiment: A and B, the fitting constants in the slip rate equation (1), and C, the pre-factor or the obstacle strength in the Taylor hardening equation (2). It was found that A and B could be fitted to reproduce the measured load-displacement response for both tips even with $C = 0$, however the lack of hardening resulted in a highly localised and smaller plastic zone compared to that observed experimentally. The addition of the hardening law ($C > 0$) produced local hardening in the plastically deformed material, promoting growth of the plastic zone. The difference in size of the plastic zone between the two indenter tip sizes is shown in Figure 3 and this disparity would have resulted in differing GND densities at a given strain and thus differing strain hardening behaviour. The slip law was dependent on the GND density (2), which is commonly used to ac-

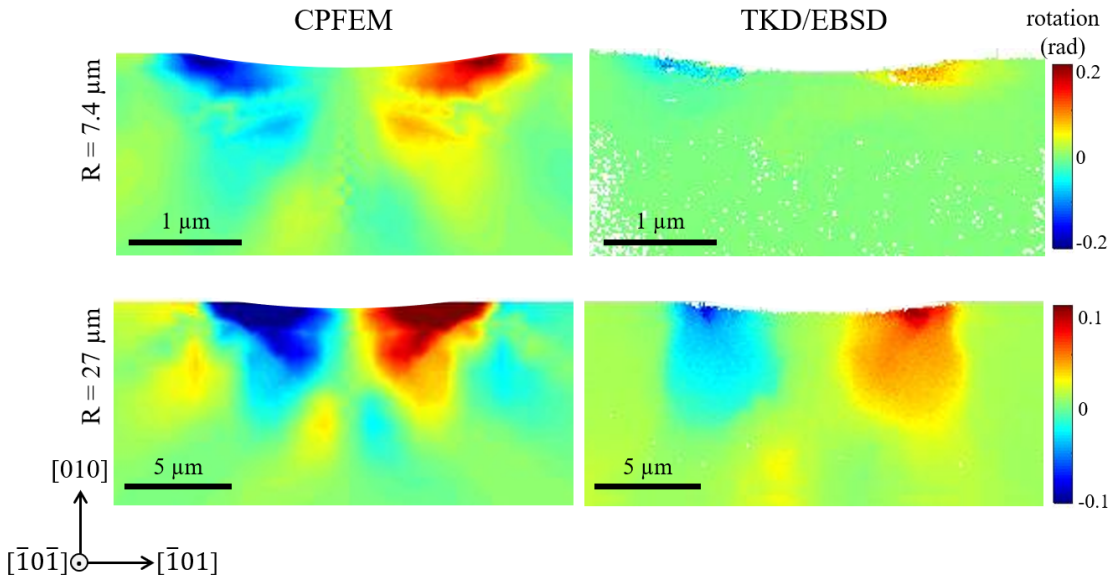

Figure 3: Infinitesimal rotations about the [$\bar{1}0\bar{1}$] axis as produced by CPFEM (left column) and CrossCourt (right column) for R=7.4 μm (top row) and R=27 μm (bottom row) indents.

count for size effects [20]. The size of the plastic zone was highly sensitive to C, where an increase in C resulted in a significant increase in the extent of the plastic zone. Note that with no GND hardening ($C = 0$) the model becomes size independent.

A value of $C = 0.05$ approximately reproduced the size of the plastic zone for the large tip by comparison and compromise between the surface profile (pile-up) and cross-sectional rotation maps. Since the obstacle strength of a dislocation cannot depend on the size of the indenter this was also used for the simulation of the small tip, however this small value of C was not sufficient to reproduce the higher hardness caused by size effects measured with the smaller tip. To overcome this, the slip law was scaled to achieve a fit to the load displacement curve by reducing the pre-factor A for the small tip. This suggests that at this scale strengthening associated with GND density was not the only mechanism responsible for the observed size effect and that other mechanisms were active.

Experimental observations showing the presence of a size effect in the measurement of a yield stress (at zero plastic strain) are plentiful [21–26]; this size effect cannot be attributed to the influence of GND density since there are no GNDs present at the initial onset of plastic strain. Additionally, a size effect has been shown for uni-axial stress states such as pillar compression, where gradients in strain and thus GNDs also do not exist. In these cases other potential size effect mechanisms are considered, including so called 'source starvation' [27] and 'source truncation' [28]. These mechanisms are associated with the activation of dislocation sources, the existence of which are indicated by the presence of discontinuities in the load displacement data. Examples of such discontinuities exist experimentally in nanoindentation [29] and micro-mechanical testing [30–32], and have also been reproduced by molecular dynamics [10] and dislocation dynamics models [26]. For indentation, this discontinuity is termed a 'pop-in' event and evidence of this is visible in Figure 1 in the load displacement data for the small indent tip reported here.

It is common that as the scale of the test decreases, the influence of the microstructure decreases and the strength approaches that of the theoretical strength of the crystal. In copper, it has been shown that the strengthening effect of a dense network of radiation induced defects is completely obscured by other strengthening mechanisms in pillar compression tests where the pillar diameter was less than 400 nm [31]. Using identical spherical indentation techniques to those used here, a similar effect was found in a sample set of CuCrZr with a significant variation in precipitate microstructure and macroscopic hardness [33]. The macro scale strength attributed to the microstructure was obscured at low values of strain and small indenter tip sizes. It was argued that the measured hardness at the small-scale was entirely dominated by the availability of dislocation sources and not influenced by microstructural features such as the precipitates or GNDs. At larger strains the trend in macroscopic hardness became apparent, which may indicate that dislocation nucleation was not a limiting mechanism due to the development of a larger dislocation structure (plastic zone). The influ-

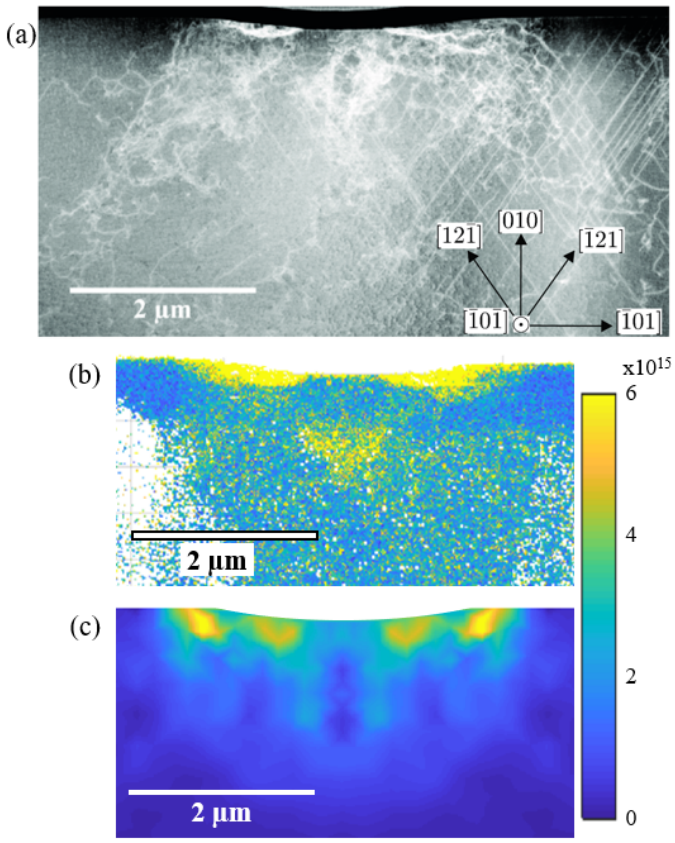

Figure 4: Comparison of the dislocation density for the R=7.4 μm indent as shown using (a) TEM, and the total GND density using (b) TKD/CrossCourt and (c) CPFEM. Slip traces are visible along $[\bar{1}21]$ at 54.7° to the horizontal and along $[12\bar{1}]$ at 125° to the horizontal. Note that the same colour scale has been used in (b) and (c) with units of m^{-2} and white pixels in (b) are un-indexed patterns.

ence and availability of dislocation sources and statistically stored dislocations (SSD) has not been accounted for in this model. The SSD density should not be neglected as can be inferred by comparing Figure 4 (a) which shows the total dislocation (GND + SSD) structure with (b) and (c), which show only the GND density. To account for these simplifications in the model the pre-factor A in the slip law had to be reduced for the small tip to reproduce the observed size effect.

As previously pointed out by Fivel et al. [34], the observations here highlight the value in the comparison of field data such as material rotations and surface relief between the model and experiment to provide a greater understanding regarding the underlying plasticity mechanisms and validity of the modelling.

It is common practise to calibrate material models by fitting the slip law parameters to reproduce the measured load displacement curve. However even for a simple three parameter model, the fitting is non-unique. Fortunately, calibrating the model to the field data now available using AFM and EBSD/TKD removes this ambiguity and allows validation of the slip and hardening laws used. As demonstrated here, the recent development of higher resolution techniques such as TKD enables the measurement of plastic deformation of smaller volumes than previously possible. Here, we use this capability to investigate the validity of using a crystal plasticity model to simulate the plastic deformation from spherical indentation on a scale of a few microns.

In this case, it was found that a hardening law associated with the evolution of GND density was not sufficient to reproduce the size effect observed experimentally, suggesting that other hardening mechanisms associated with dislocation source activation and statistically stored dislocations were present. Inclusion of these additional mechanisms in the crystal plasticity model will be considered as part of future work.

This project has received funding from the EMPIR programme co-nanced by the Participating States and from the European Unions Horizon 2020 research and innovation programme. Equipment at the Materials Research Facility at UKAEA was used; the MRF is funded by the UK National Nuclear User Facility and Henry Royce Institute. Thanks to the University of Manchesters School of Materials for access to TEM facilities and support. ET would like to thank EPSRC for financial support through an Early Career Fellowship EP/N007239/1.toftuk

[1] T. J. Bell, J. S. Field, M. V. Swain, Thin Solid Films 220 (1992) 289–294. doi:10.1016/0040-6090(92)90587-2.
[2] C. D. Hardie, S. G. Roberts, J. Nucl. Mater. 433 (1-3) (2013) 174–179. doi:10.1016/j.jnucmat.2012.09.003.
[3] C. Motz, T. Schöberl, R. Pippan, Acta Mater. 53 (2005) 4269–4279. doi:10.1016/j.actamat.2005.05.036.
[4] M. D. Uchic, P. A. Shade, D. M. Dimiduk, Annu. Rev. Mater. Res. 39 (2009) 361–386. doi:10.1146/annurev-matsci-082908-145422.
[5] M. Beghini, L. Bertini, V. Fontanari, Int. J. Solids Struct. 43 (2006) 2441–2459. doi:10.1016/j.ijsolstr.2005.06.068.
[6] D. L. Krumwiede, T. Yamamoto, T. A. Saleh, S. A. Maloy, G. R. Odette, P. Hosemann, J. Nucl. Mater. 504 (2018) 135–143. doi:10.1016/j.jnucmat.2018.03.021.
[7] O. Casals, J. Ocenasek, J. Alcala, Acta Mater. 55 (1) (2007) 55–68. doi:10.1016/j.actamat.2006.07.018.
[8] J. W. Kysar, Y. X. Gan, T. L. Morse, X. Chen, M. E. Jones, J. Mech. Phys. Solids 55 (7) (2007) 1554–1573. doi:10.1016/j.jmps.2006.09.009.
[9] S. Kucharski, S. Stupkiewicz, H. Petryk, Exp. Mech. 54 (6) (2014) 957–969. doi:10.1007/s11340-014-9883-1.
[10] H.-J. Chang, M. Fivel, D. Rodney, M. Verdier, Comptes Rendus Phys. 11 (3-4) (2010) 285–292. doi:10.1016/j.crhy.2010.07.007.
[11] K. R. Narayanan, S. Subbiah, I. Sridhar, Appl. Phys. A Mater. Sci. Process. 105 (2) (2011) 453–461. doi:10.1007/s00339-011-6618-3.

[12] N. Zaafarani, D. Raabe, R. N. Singh, F. Roters, S. Zaefferer, Acta Mater. 54 (7) (2006) 1863–1876. doi:10.1016/j.actamat.2005.12.014.
[13] N. Zaafarani, D. Raabe, F. Roters, S. Zaefferer, Acta Mater. 56 (1) (2008) 31–42. doi:10.1016/j.actamat.2007.09.001.
[14] X. Z. Liang, M. F. Dodge, J. Jiang, H. B. Dong, Ultramicroscopy 197 (2019) 39–45. doi:10.1016/j.ultramic.2018.11.011.
[15] J. H. O'Connell, M. E. Lee, J. Westraadt, J. A. A. Engelbrecht, Phys. B Condens. Matter 535 (2018) 293–298. doi:10.1016/j.physb.2017.08.005.
[16] H. Yu, J. Liu, P. Karamched, A. J. Wilkinson, F. Hofmann, Scr. Mater. 164 (2019) 36–41. doi:10.1016/j.scriptamat.2018.12.039.
[17] F. P. E. Dunne, D. Rugg, A. Walker, Int. J. Plast. 23 (6) (2007) 1061–1083. doi:10.1016/j.ijplas.2006.10.013.
[18] Z. Wang, H. Bei, E. P. George, G. M. Pharr, Scr. Mater. 65 (6) (2011) 469–472. doi:10.1016/j.scriptamat.2011.05.030.
[19] V. Kuksenko, S. Roberts, E. Tarleton, Int. J. Plast.doi:10.1016/j.ijplas.2018.12.008.
[20] W. D. Nix, H. Gao, J. Mech. Phys. Solids 46 (3) (1998) 411–425. doi:10.1016/S0022-5096(97)00086-0.
[21] E. Arzt, Acta Mater. 46 (16) (1998) 5611–5626. doi:10.1016/S1359-6454(98)00231-6.
[22] M. D. Uchic, D. M. Dimiduk, J. N. Florando, W. D. Nix, Science (80-.). 305 (5686) (2004) 986–989. doi:10.1126/science.1098993.
[23] G. M. Pharr, E. G. Herbert, Y. Gao, Annu. Rev. Mater. Res. 40 (2010) 271–292. doi:10.1146/annurev-matsci-070909-104456.
[24] O. Kraft, P. A. Gruber, R. Mönig, D. Weygand, Annu. Rev. Mater. Res. 40 (2010) 293–317. doi:10.1146/annurev-matsci-082908-145409.
[25] D. J. Dunstan, A. J. Bushby, Int. J. Plast. 40 (2013) 152–162. doi:10.1016/j.ijplas.2012.08.002.
[26] E. Tarleton, D. S. Balint, J. Gong, A. J. Wilkinson, Acta Mater. 88 (2015) 271–282. doi:10.1016/j.actamat.2015.01.030.
[27] J. R. Greer, W. C. Oliver, W. D. Nix, Acta Mater. 53 (6) (2005) 1821–1830. doi:10.1016/j.actamat.2004.12.031.
[28] T. A. Parthasarathy, S. I. Rao, D. M. Dimiduk, M. D. Uchic, D. R. Trinkle, Scr. Mater. 56 (4) (2007) 313–316. doi:10.1016/j.scriptamat.2006.09.016.
[29] C. D. Hardie, S. G. Roberts, A. J. Bushby, J. Nucl. Mater. 462 (2015) 391–401. doi:10.1016/j.jnucmat.2014.11.066.
[30] D. E. J. Armstrong, C. D. Hardie, J. Gibson, A. J. Bushby, P. D. Edmondson, S. G. Roberts, J. Nucl. Mater. 462 (2015) 374–381. doi:10.1016/j.jnucmat.2015.01.053.
[31] D. Kiener, P. Hosemann, S. A. Maloy, A. M. Minor, Nat. Mater. 10 (8) (2011) 608. doi:10.1038/nmat3055.
[32] J. R. Greer, J. T. M. De Hosson, Prog. Mater. Sci. 56 (6) (2011) 654–724. doi:10.1016/j.pmatsci.2011.01.005.
[33] A. J. Cackett, J. J. H. Lim, P. Klupś, A. J. Bushby, C. D. Hardie, J. Nucl. Mater.doi:10.1016/j.jnucmat.2018.04.012.
[34] M. C. Fivel, C. F. Robertson, G. R. Canova, L. Boulanger, Acta Mater. 46 (17) (1998) 6183–6194. doi:10.1016/j.crhy.2010.07.007.

Supplementary Materials

S1. Methods

S1.1. Sample Preparation

A high purity (99.999%) single-crystal Cu sample with surface normal, n = [010], from Goodfellow was used for this work. Standard mechanical polishing was performed with a series of SiC abrasive paper of incrementally decreasing grit sizes (final stage: grit size 2.5 μm) followed by electropolishing for 10 s with Struers D2 electrolyte. This resulted in a flat surface with minimal induced deformation, as is ideally required for nanoindentation. Finally, the sample was fixed to an aluminium pin stub so that it could be mounted in both the nanoindenter and focused ion beam (FIB). Whilst not in use the sample was stored in a vacuum desiccator to minimise any oxidation.

S1.2. Nanoindentation

Nanoindentation was performed using an Agilent (now Keysight) G200 nanoindenter and two spherical tips were used with tip radii, R, of 7.4 and 27 μm (as measured using the calibration routine fully described in the appendix of [S1]). Load displacement data was obtained using a method similar to that of Field and Swain's [S2]; multiple load - partial unload cycles of incrementally increasing maximum load are applied to enable the measurement of material properties as a function of penetration depth. In this work 40 cycles were used and both indents were made to an indentation strain of $\varepsilon = 0.2$, which was defined as follows. If it is assumed that unloading is elastic, Hertzian contact mechanics [S3] can be used to calculate the radius of residual impression, h_r, for every load cycle by fitting to the unload curve data and extrapolating back to the x-axis of a load displacement plot. This, in addition to the measured indentation depth at maximum load, h_1, can then be used to calculate the contact depth,

$$h_c = \frac{h_1 + h_r}{2} \tag{S1}$$

and therefore the contact radius, which is found geometrically to be,

$$a = \sqrt{2Rh_c - h_c^2} \tag{S2}$$

Indentation strain is then defined as the ratio between contact radius, a, and tip radius, R,

$$\varepsilon = \frac{a}{R} \tag{S3}$$

S1.3. Atomic force microscopy

Atomic force microscopy (AFM) was used to characterise the surface deformation (pile-up) around both indents. A Veeco Dimension 3000 AFM in contact mode was used to acquire square maps with areas of 8 and 30 μm^2, centred on the residual indents from the tips with R=7.4 μm and R=27 μm, respectively. Post-processing was carried out using tools contained within open-source software Gwyddion [S4]: row alignment, correction of horizontal scars and interpolation of small defects (i.e. surface contamination). Care was taken to not alter the size and shape of the indentation pit and pile-up regions during this stage.

S1.4. Diffraction (TKD/EBSD)

Cross-sectional lamellae for TKD and EBSD analyses were produced using a FEI Helios 600i NanoLab dual beam SEM/FIB equipped with a Ga ion source. The preparation technique was similar to the FIB lift-out technique described by Giannuzzi and Stevie in [S5]. Final thinning/polishing was done once the lamella was mounted in a copper TEM grid and held in place with platinum. In order to remove any ion-beam damage (curtaining, Ga ion implantation) from previous stages, a beam voltage of 2 kV was used to perform final cleaning of the lamella with the sample positioned at 7° to the beam. Such a high angle is acceptable when operating with a low voltage since the ions can only implant into the material ~2 nm [S6]. For TKD this polishing was carried out on both sides of the lamella until electron transparency at 5 kV was achieved. For EBSD only one side was polished, leaving a final thickness of ~1 μm.

Once the samples had been thinned as described above, they were manually transferred from the FIB into a sample holder specifically designed for TKD (manufactured by Oxford Instruments), which clamps the TEM grid between two plates. This holder was then mounted on a post in the scanning electron microscope (SEM) angled at either 70° or −20° from horizontal, in order to carry out EBSD or TKD, respectively (see Figure S1). TKD was chosen to image the 7.4 μm indent because of the significantly better longitudinal resolution possible compared to EBSD. The height of the SEM stage could be varied to avoid shadowing and obtain the best pattern quality. All experiments were carried out in a TESCAN Mira3 XMH FEG-SEM microscope equipped with a NordlysMax2 camera from Oxford Instruments. Kikuchi patterns were collected and processed using AZtec 2.3 EBSD software, also from Oxford Instruments. The electron beam was operated at the maximum 30 kV since this yields a higher in-

tensity of transmitted electrons through the film and therefore produced the brightest diffraction patterns.

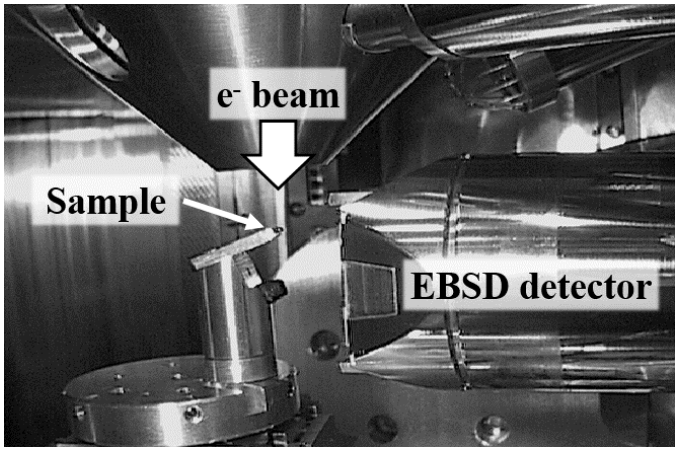

Figure S1: Arrangement in SEM when carrying out TKD

Stress and elastic strain measurements were made using CrossCourt 4 [S7], a software that calculates small lattice rotations and distortions using cross-correlation of Kikuchi patterns acquired at high resolution [S8]. The theory behind this software has been extensively described elsewhere [S9–S11] so will not be repeated here, but in essence it exploits the fact that a change in elastic strain necessitates a change in lattice plane spacing, which is observed as a change in position of Kikuchi bands. Likewise, a small lattice rotation, i.e. a change in crystal orientation, shifts the whole pattern. Minute variations between multiple regions of interest in two patterns can be measured using cross-correlation and this results in subpixel accuracy measurements of the pattern shift and thus high strain sensitivity. This technique was used to measure and map the in-plane infinitesimal rotation ω_{12} (rotations about the x_3 axis, $[\bar{1}0\bar{1}]$) was used for comparison with the model.

S1.5. Transmission electron microscopy

Scanning transmission electron microscopy (STEM) was performed using a 200 kV FEI Talos at the University of Manchester School of Materials. Bright- and dark-field images were acquired with the sample tilted such that the incident beam was down the [101] zone axis. Dislocations can easily be seen in this mode since the bending of the crystal lattice around them changes the diffraction condition and produces strong diffraction contrast. Accompanying diffraction patterns were collected to capture information on the imaging conditions. For this analysis only the R=7.4 μm indent was looked at. This was due to significant bending of the foil during thinning of the R=27 μm indent, which consequently meant it was not possible to achieve a thin enough sample for TEM.

S1.6. Crystal plasticity model

A strain gradient crystal plasticity user material (UMAT) for Abaqus was developed based on the (user element) UEL originally written by Dunne et al. [S12, S13]. The deformation is decomposed multiplicatively into a plastic, $\boldsymbol{F}^p$, and elastic, $\boldsymbol{F}^e$, deformation gradient

$$\boldsymbol{F} = \boldsymbol{F}^e \boldsymbol{F}^p \tag{S4}$$

the flow rule has the form

$$\dot{\boldsymbol{F}}^p = \boldsymbol{L}^p \boldsymbol{F}^p \tag{S5}$$

Where the plastic velocity gradient, $\boldsymbol{L}^p$, is given by the crystallographic strain rate resulting from dislocation glide on the active slip systems with slip direction $\boldsymbol{s}^k$ and slip plane normal $\boldsymbol{n}^k$

$$\boldsymbol{L}^p = \sum_{k=1}^{k=12} \dot{\gamma}^k \boldsymbol{s}^k \otimes \boldsymbol{n}^k \tag{S6}$$

The crystallographic slip rate $\dot{\gamma}$ is given by

$$\dot{\gamma}^k = A \sinh\left(B(|\tau^k| - \tau_c^k)\right) \mathrm{sgn}(\tau^k) \tag{S7}$$

for $|\tau^k| > \tau_c^k$ and $\dot{\gamma}^k = 0$ otherwise, where the CRSS is

$$\tau_c^k(\rho_c^k) = \tau_c^0 + C\mu b \sqrt{\rho_c^k} \tag{S8}$$

A, B and C are treated here as fitting constants. It is interesting to compare this slip law to the more commonly used power law of the form $\dot{\gamma}^k = \dot{\gamma}_0(\tau^k/s^k)^m$ so that $A \sim \dot{\gamma}_0$, the reference shear rate and $B \sim 1/s^k$ the initial slip resistance. Typical values used for copper are then $A \sim 10^{-3}$ s^{-1} and $B \sim 0.1$ [S14]. The fitting parameters A and B can also be related to more fundamental quantities, $A = \rho_m b^2 f \exp(-\Delta F/k_b T)$ and $B = V/k_b T$. Typical values used in the literature are of the order $\rho_m \sim 1\ \mu\mathrm{m}^{-2}$, for the mobile dislocation density which we are implicitly assuming to be constant. The attempt frequency, $f \sim 10^{11}$ s^{-1}, activation volume $V \sim 50b^3$ and Helmholtz free energy, $\Delta F \sim 0.5$ eV, indicate $A \sim 10^{-5}$ s^{-1} and $B \sim 0.2$. The resolved shear stress is $\tau = \boldsymbol{s} \cdot \boldsymbol{\sigma} \cdot \boldsymbol{n}$, τ_c is the critically resolved shear stress and ρ_c^k is the dislocation density which cuts the slip plane of slip system k,

$$\rho_c^k = \sum_{j=1}^{j=18} |\boldsymbol{l}^j \cdot \boldsymbol{n}^k| \rho_{GND}^j \tag{S9}$$

where $\boldsymbol{l}$ is the dislocation line direction and $\boldsymbol{n}$ is the slip plane normal and in our model only GNDs, ρ_{GND}, are considered. In FCC materials there are a total of 12 edge and 6 screw dislocation densities. Each of the 4 (111) slip planes are intersected by 3 screw and 6 edge dislocation densities. The 18 GND densities are obtained by solving using the right pseudo inverse

$$\boldsymbol{A}\boldsymbol{\rho}_{GND} = \boldsymbol{G} \tag{S10}$$

where column j of $\boldsymbol{A}$ is formed by reshaping the tensor product of $\boldsymbol{l}^j \otimes \boldsymbol{b}^j$ of the dislocation line direction and Burgers vector for slip system j into a column vector. The right hand side is the dislocation density tensor defined by [S15]

$$G_{km} = (\nabla \times \boldsymbol{F}^p)_{km} = \epsilon_{ijk} \frac{\partial F^p_{mj}}{\partial X_i} \tag{S11}$$

also reformatted as a column vector. As $\boldsymbol{A}$ is not square it can not be inverted, instead the pseudo right inverse is found which allows (the L2 minimum) solution for the density vector to be easily obtained

$$\boldsymbol{A}^{-r} = \boldsymbol{A}^T(\boldsymbol{A}\boldsymbol{A}^T)^{-1}, \tag{S12}$$

where $\boldsymbol{A}\boldsymbol{A}^{-r} = \boldsymbol{I}$ which allows (the L2 minimum) solution for the GND density vector $\boldsymbol{\rho}_{GND}$ to be obtained immediately

$$\boldsymbol{\rho} = \boldsymbol{A}^{-r}\boldsymbol{G} \tag{S13}$$

To allow the curl of the plastic deformation gradient to be calculated within a UMAT, the initial gauss point coordinates and current value of $\boldsymbol{F}^p$ at every integration point was stored in a common block; protected using the Abaqus utility subroutine `MutexLock()` to take advantage of the Abaqus parallelisation. The stress is updated at each time increment using Newton iteration,

$$\boldsymbol{\sigma}^{t+\Delta t} = \boldsymbol{\sigma}^{trial} - \boldsymbol{C}\boldsymbol{D}^p(\boldsymbol{\sigma}^{t+\Delta t})\Delta t \tag{S14}$$

$$\boldsymbol{\sigma}^{trial} = \boldsymbol{\sigma}^t + \left(\boldsymbol{C}\boldsymbol{D} + \boldsymbol{W}^t\boldsymbol{\sigma}^t - \boldsymbol{\sigma}^t\boldsymbol{W}^t\right)\Delta t \tag{S15}$$

where $\boldsymbol{W} = \frac{1}{2}\left(\boldsymbol{L} - \boldsymbol{L}^T\right)$ is the spin tensor, $\boldsymbol{D} = \frac{1}{2}\left(\boldsymbol{L} + \boldsymbol{L}^T\right)$ is the rate of deformation tensor and $\boldsymbol{C}$ is the elastic stiffness matrix in Voigt notation for pure copper. The stress is updated in the Newton loop for each iteration i using [S12]

$$\boldsymbol{\sigma}^{t+\Delta t}_{i+1} = \boldsymbol{\sigma}^{t+\Delta t}_i + \delta\boldsymbol{\sigma}_i \tag{S16}$$

where the stress increment is

$$\delta\boldsymbol{\sigma}_i = \left[\boldsymbol{I} + \boldsymbol{C}\frac{\partial \boldsymbol{D}^p}{\partial \boldsymbol{\sigma}}\Delta t\right]^{-1}\left[\boldsymbol{\sigma}^{trial} - \boldsymbol{\sigma}^{t+\Delta t}_i - \boldsymbol{C} : \boldsymbol{D}^p(\sigma^{t+\Delta t}_i)\Delta t\right] \tag{S17}$$

where the plastic deformation rate is

$$\boldsymbol{D}^p = \mathrm{sym}\left(\sum_k A \sinh\left(B(|\tau^k| - \tau^k_c)\right)\boldsymbol{s}^k \otimes \boldsymbol{n}^k\right)$$

with the following derivative in stress

$$\frac{\partial \boldsymbol{D}^p}{\partial \boldsymbol{\sigma}} = \mathrm{sym}\left(\sum_k AB\cosh\left(B(|\tau^k| - \tau^k_c)\right)[\boldsymbol{s}^k \otimes \boldsymbol{n}^k] \otimes [\boldsymbol{n}^k \otimes \boldsymbol{s}^k]\right) \tag{S18}$$

The model parameters varied slightly for the two indent sizes. A total of 50.6k and 54.8k quadratic hexahedral elements with reduced integration (C3D20R) were used to mesh cubes of side length, L, 41 μm and 150 μm for the R=7.4 μm and R=27 μm indents, respectively. Each mesh was biased, reducing to 0.25 μm and 1 μm under the indenter tips, which were modelled as rigid parts with perfect geometry of radii 7.4 μm and 27 μm. The small sliding node to surface contact algorithm was used with the default frictionless hard contact property. Symmetry boundary conditions were applied to the faces $x = 0$ and $y = 0$ so that only one quarter of the block was simulated. The top surface (being indented) and faces at $x = L$ and $y = L$ were traction free while the bottom surface was fixed. Elastic anisotropy was used with the parameters shown in Table 1 with the model axis aligned along $x = [\bar{1}01]$, $y = [010]$, $z = [\bar{1}0\bar{1}]$ with the indenter displaced along y by distances, U, of 0.14 μm and 0.61 μm for the small and large indents respectively.

[S1] T. T. Zhu, A. J. Bushby, D. J. Dunstan, J. Mech. Phys. Solids 56 (2008) 1170–1185. doi:10.1016/j.jmps.2007.10.003.

[S2] J. S. Field, M. V. Swain, J. Mater. Res. 8 (2) (1993) 297–306. doi:10.1557/JMR.1993.0297.

[S3] H. Hertz, J. fur die Reine und Angew. Math.arXiv:cu31924012500306, doi:10.1515/crll.1882.92.156.

[S4] D. Nečas, P. Klapetek, Cent. Eur. J. Phys. 10 (1) (2012) 181–188. doi:10.2478/s11534-011-0096-2.

[S5] L. A. Giannuzzi, F. A. Stevie, Micron 30 (3) (1999) 197–204. doi:10.1016/S0968-4328(99)00005-0.

[S6] J. Mayer, L. a. Giannuzzi, T. Kamino, J. Michael, MRS Bull. 32 (05) (2007) 400–407. doi:10.1557/mrs2007.63.

[S7] [link]. URL `http://www.hrebsd.com/wp/crosscourt/`

[S8] A. J. Wilkinson, Ultramicroscopy 62 (4) (1996) 237–247. doi:10.1016/0304-3991(95)00152-2.

[S9] A. J. Wilkinson, G. Meaden, D. J. Dingley, Ultramicroscopy 106 (2006) 307–313. doi:10.1016/j.ultramic.2005.10.001.

[S10] T. B. Britton, A. J. Wilkinson, Ultramicroscopy 111 (8) (2011) 1395–1404. doi:10.1016/j.ultramic.2011.05.007.

[S11] A. J. Wilkinson, T. B. Britton, J. Jiang, P. S. Karamched, IOP Conf. Ser. Mater. Sci. Eng. 55 (2014) 12020. doi:10.1088/1757-899X/55/1/012020.

[S12] F. P. E. Dunne, D. Rugg, A. Walker, Int. J. Plast. 23 (6) (2007) 1061–1083. doi:10.1016/j.ijplas.2006.10.013.

[S13] F. P. E. Dunne, R. Kiwanuka, A. J. Wilkinson, Proc. R. Soc. A Math. Phys. Eng. Sci. 468 (2145) (2012) 2509–2531. doi:10.1098/rspa.2012.0050.

[S14] N. Zaafarani, D. Raabe, R. N. Singh, F. Roters, S. Zaefferer, Acta Mater. 54 (7) (2006) 1863–1876. doi:10.1016/j.actamat.2005.12.014.

[S15] S. Das, F. Hofmann, E. Tarleton, Int. J. Plast.doi:https://doi.org/10.1016/j.ijplas.2018.05.001.